North Pacific Decadal Variability in the GEOS-5 Atmosphere-Ocean Model

Deepthi Achuthavarier
Goddard Earth Sciences Technology and Research, Universities Space Research Association, Columbia, MD

Siegfried D. Schubert
Global Modeling and Assimilation Office, NASA Goddard Space Flight Center, Greenbelt, MD

Yury V. Vikhliaev
Goddard Earth Sciences Technology and Research, Universities Space Research Association, Columbia, MD

Submitted to Journal of Climate
Oct 25, 2013

Corresponding author's address:
Deepthi Achuthavarier
GESTAR/USRA
Global Modeling and Assimilation Office, Code 610.1, Bldg. 33
NASA Goddard Space Flight Center, Greenbelt, MD 20771
Email: deepthi.achuthavarier@nasa.gov
Phone: 301-614-5854.

Abstract

This study examines the mechanisms of the Pacific decadal oscillation (PDO) in the GEOS-5 general circulation model. The model simulates a realistic PDO pattern that is resolved as the first empirical orthogonal function (EOF) of winter sea surface temperature (SST). The simulated PDO is primarily forced by Aleutian low through Ekman transport and surface fluxes, and shows a red spectrum without any preferred periodicity. This differs from the observations, which indicate a greater role of El Nino-Southern Oscillation (ENSO) forcing, and likely reflects the too short time scale of the simulated ENSO. The geostrophic transport in response to the Aleutian low is limited to the Kuroshio-Oyashio Extension, and is unlikely the main controlling factor in this model, although it reinforces the Ekman-induced SST anomalies. The delay between the Aleutian low and the PDO is relatively short (1 year) suggesting that the fast Ekman response (rather than Rossby wave propagation) sets the SST pattern immediately following an Aleutian low fluctuation. The atmospheric feedback (response to the SST) is only about 25% of the forcing and never evolves into an Aleutian low completely, instead projecting onto the North Pacific Oscillation (NPO), a meridional dipole in sea level pressure (SLP). The lack of preferred periodicity and weak atmospheric response both indicate a coupled oscillation is an unlikely mechanism for the PDO in this model. In agreement with recent studies, the NPO is correlated with the North Pacific Gyre Oscillation (NPGO), which is another leading EOF of the North Pacific SST. A possible connection between the PDO and the NPGO is discussed.

1. Introduction

The dominant pattern of sea surface temperature (SST) variability in the extra-tropical Pacific is characterized by same-signed anomalies in the central and western parts of the basin and opposite signed anomalies along the west coast of the United States and the Gulf of Alaska, and is commonly referred as the Pacific decadal oscillation (PDO) or variability (Trenberth and Hurrell 1994; Mantua et al. 1997; Zhang et al. 1997). This pattern exhibits decadal to multi-decadal variability with marked 'regime shifts' around 1925, 1947 and 1976 along with interannual variability that is largely in tune with the tropical El Niño-Southern Oscillation (ENSO) phenomenon. The decadal spectral peaks of the associated time series are broad and weak in the observational records, and therefore, the existence of a preferred oscillation is unclear (see, e.g., reviews by Miller and Schneider 2000; Liu et al. 2012). Nevertheless, pronounced low-frequency variability is apparent. A positive (negative) phase of the PDO is defined as the period when the eastern Pacific is anomalously warm (cool) and the central and the west Pacific is anomalously cool (warm) and is accompanied by negative (positive) sea level pressure (SLP) anomalies over the Aleutian Islands.

The PDO appears to force atmospheric teleconnection patterns controlling climate variability in distant locations (Trenberth and Hurrell 1994; Mantua et al. 1997; Deser et al. 2004). For example, a positive phase of PDO coincides with enhanced wintertime precipitation over Alaska, southern United States and northern Mexico, reduced precipitation over much of the interior United States, and warm winter air temperature and reduced snowpack in the Pacific Northwest (Mantua et al. 1997). These

teleconnection patterns may be useful in seasonal and interannual prediction efforts in those regions. Additionally, understanding the relative role of natural decadal modes like the PDO and the anthropogenic warming trend is important for near-term decadal prediction.

A widely recognized model for the excitation of low frequency variability in extra-tropical oceans, in general, is that of the stochastic noise forcing (Hasselmann 1976), where SST variability is solely forced by the atmospheric 'noise'. The 'noise' stands for atmospheric variability that is not forced by SST or other boundary states. In its simplest form, this model proposes that an atmospheric heat flux of white spectrum when coupled to a slab ocean model produces low frequency SST variability as the input heat flux is slowly damped due to the large heat capacity of the ocean. The resulting SST spectrum is red without any preferred periodicity. Extensions of this model include a propagative stochastic model where advection or wave propagation is taken into account (Frankignoul et al. 1997; Jin 1997; Saravanan and McWilliams 1997) and stochastically driven ocean dynamics model (Schneider et al. 2002).

Another possibility is that the PDO is forced by ENSO through its atmospheric teleconnection to the North Pacific (Trenberth and Hurrell 1994; Zhang et al. 1997; Newman et al. 2003; Deser et al. 2004; Vimont 2005; Alexander and Scott 2008). This idea is supported by the observation that the two patterns are largely similar and the two modes underwent major decadal regime shifts in the observed records (Deser et al. 2004). The ENSO-forced atmospheric circulation patterns can generate SST anomalies in the

119 north-central Pacific on the seasonal timescale. These SST anomalies gain maximum
120 amplitude in the spring following an ENSO mature phase, and can be stored beneath the
121 mixed layer and resurfaced in the next winter via 'reemergence' (Alexander et al. 1999).
122 The reemergence mechanism acts to enhance the persistence of SST anomalies from
123 winter-to-winter thereby aiding in the reddening process (Deser et al. 2003). Thus the
124 ENSO forced circulation anomalies can be considered as a 'signal' in the white noise-
125 atmosphere that imparts temperature anomalies at quasi-regular intervals which has some
126 persistence in the North Pacific Ocean mixed layer. Newman et al. (2003) showed that a
127 first order autoregressive model (AR1) with an ENSO forcing forecasts the observed
128 PDO with remarkable skill. Another viewpoint is that the PDO is due to the decadal
129 modulation of ENSO, and therefore a statistical residue of ENSO on decadal timescales
130 (Zhang et al. 1997; Vimont 2005).
131
132 Latif and Barnett (1994) proposed that mid-latitude atmosphere-ocean interaction
133 together with westward propagating oceanic Rossby waves could support a self-sustained
134 decadal oscillation. Their proposal begins by assuming an SST anomaly in the Kuroshio-
135 Oyashio extension (KOE) region of the subtropical gyre. This subsequently grows
136 through Bjerknes-like ocean-atmosphere feedback and imparts a wind stress pattern in
137 the central Pacific that in turn results in Ekman transport and Rossby wave propagation
138 from the central Pacific to the western boundary. The resulting gyre anomalies eventually
139 replace the original KOE SST anomalies with that of opposite sign. However, there is
140 now a general consensus from observations and general circulation models (GCMs) that
141 the central Pacific wind stress anomalies in fact lead the KOE SST and therefore are

142 unlikely due to an oceanic forcing (Schneider et al. 2002). This leads to a modified Latif-
143 Barnett model in which a basin scale wind stress pattern with its maximum slightly
144 shifted to the east of dateline forces oceanic Rossby waves in the central Pacific which
145 generates KOE SST anomalies after 4-5 years (Deser et al. 1996; Miller et al. 1998;
146 Schneider et al. 2002). The wind stress pattern is associated with the sea level pressure
147 (SLP) anomalies of the Aleutian low. In this case, whether or not a closed oscillation
148 occurs depends on if and how the atmosphere responds to the KOE SST. If the
149 atmospheric response reverses the sign of the original wind stress curl anomalies, a
150 coupled self-sustained oscillation may evolve. Results from the NCAR CCSM2.0
151 (Known and Deser 2007) suggest that the PDO in that model is in agreement with the
152 Aleutian low-induced Rossby wave mechanism.
153
154 The length of observational records is a main constraint in evaluating these mechanisms,
155 and it may be helpful to analyze long simulations of the atmosphere-ocean general
156 circulation models (AOGCM), which are increasingly becoming computationally
157 cheaper. In this study, we take advantage of a 350-year long simulation of the Goddard
158 Earth Observing System (GEOS-5) AOGCM to examine the characteristics and
159 mechanisms of the PDO. We will first examine the relative importance of the tropical
160 versus extra-tropical forcing on the PDO – i.e., to what extent the ENSO-forced SST
161 anomalies are reflected in the PDO. Secondly, we will examine the role of midlatitude
162 atmospheric variability and the relative roles of surface heat flux, Ekman and geostrophic
163 advection terms. In doing so, we hope to quantify the relative contributions to the PDO of
164 a fast local response that occurs through surface heat flux and Ekman layer advection and

165 a delayed remote response at the KOE region, involving geostrophic adjustments which
166 is indicative of the wind stress curl induced Rossby wave mechanism.
167
168 While most previous studies of Pacific decadal variability have focused on the PDO,
169 which is usually resolved as the first EOF of North Pacific SST variability, some recent
170 studies have pointed out the importance of the second EOF (Bond et al. 2003),
171 particularly in the years after the 1976 decadal shift. Di Lorenzo et al. (2008) found that
172 the second EOF is connected to the eastern and central branches of the subtropical gyre
173 and is often referred to as the North Pacific Gyre Oscillation (NPGO). In this study, we
174 will briefly touch upon the NPGO in GEOS-5 and its potential connection with the PDO.
175
176 Section 2 describes the model and observational data. Section 3 discusses the results,
177 which include a brief summary of the mean climate (3.1), the spatial and temporal
178 characteristics of the PDO and the NPGO (3.2), the tropical connection of the PDO (3.3),
179 and extra-tropical atmospheric forcing and air-sea feedback (3.4). The summary and
180 discussion is provided in Section 4.
181
182 **2. Model and data**
183
184 The atmospheric component of the GEOS-5 AOGCM was developed at NASA's Global
185 Modeling and Assimilation Office (Rienecker et al. 2008; Molod et al. 2012). Some key
186 components of the model physics include the Relaxed Arakawa-Schubert scheme for
187 convection (Moorthi and Suarez 1992), a Monin-Obukhov surface layer, which includes

188 the effects of a viscous sublayer for heat and moisture transport (Helfand and Schubert
189 1995), and turbulence schemes by Lock (2000) and Louis and Geleyn (1982). The Ocean
190 component is the Modular Ocean Model Version 4 (MOM4) developed by the
191 Geophysical Fluid Dynamics Laboratory (Griffies et al. 2005), and the sea ice model is
192 the Los Alamos sea ice model (CICE) (Hunke and Lipscomp 2008). The land surface
193 model is a catchment-based scheme (Koster et al. 2000) that accounts for sub-grid scale
194 heterogeneity in surface moisture.

195 The resolution of the atmospheric model is 2.5° longitude by 2° latitude with 72 vertical
196 layers and that of the ocean is 1° in longitude and latitude telescoping to 1/3° meridional
197 spacing near the equator, with 50 vertical levels. The ocean vertical grid spacing is a
198 constant 10 m over the top 225 m. The current simulation was started from an earlier run
199 where the atmospheric model was initialized from an uncoupled run forced by observed
200 SST. The ocean model was initialized with climatological temperature and salinity from
201 Levitus and Boyer (1994a;b). Green house gas concentrations are fixed at 1950's level.
202 In this study, we examine the last 350 years from a 407-year long single coupled run.
203 The first 57 years are omitted as model spin-up, as determined by visual examination of
204 the globally averaged annual mean SST.

205 The model results are compared with observed SST product of Rayner et al. (2003) for
206 the period 1870-2011 and sea level pressure (SLP) for the period 1871-2010 from the
207 NOAA 20th century reanalysis (Compo et al. 2011). A global warming signal was
208 removed from the observed SST by linear de-trending. Oceanic variables from the model
209 are also de-trended to eliminate any model drift. Monthly or seasonal anomalies are
210 obtained by removing their respective long-term mean values. A 6-year low-pass Lanczos

211 filter (Duchon, 1979) is utilized in certain analyses to better extract the decadal signals.
212 Diagnostic tools include Empirical Orthogonal function (EOF) decomposition, spectral
213 analysis, and lag correlation or regression. The statistical significance of the spectral
214 peaks is estimated with a Chi-squared test with respect to a null hypothesis based on an
215 AR1 red noise process. A two-sided t-test is used to assess significance of temporal
216 correlation coefficients. The effective number of degrees of freedom for the t-test is
217 calculated as, $N' = N\left(\frac{1-r_{1x}r_{1y}}{1+r_{1x}r_{1y}}\right)$, where N is the number of time steps in the data, N' is
218 the effective number of degrees of freedom and r_{1x} and r_{1y} are the lag-1 autocorrelation
219 coefficients for time series x and y, respectively (Bretherton et al. 1999).

220 **3. Results**

221 **3.1. Mean climate**

222 The GEOS-5 AOGCM produces a stable, realistic mean state, and realistic major modes
223 of variability (Vikhliaev et al. 2011). This is confirmed in the current 350-year long
224 simulation. For example, Fig. 1 shows that the model captures the climatological features
225 of the tropical SST such as the Pacific warm pool and cold tongue fairly well. Some
226 errors in the model are common to many current climate models and they include the
227 westward extension of the cold tongue, which often results in a 'double ITCZ' pattern in
228 precipitation, warm bias along the continental coasts, and a meridionally confined ENSO
229 that extends too far to the west. The double ITCZ problem is often related to errors in
230 atmosphere-ocean feedbacks in the tropical Pacific (Sun et al. 2003). The warm bias over
231 the western side of the continents is likely due to the lack of low clouds in this model
232 (Molod et al. 2012) or coastal upwelling biases prevalent in AOGCMs in general (e.g.,

233 Griffies et al. 2009). The enhanced variance in the tropical Indian Ocean implies an
234 unrealistically strong forcing from the Pacific, which may be due to the westward
235 extension of the ENSO.
236
237 **3.2. Low frequency variability in North Pacific SST**
238
239 In this section, we describe the leading patterns of variance in the North Pacific SST that
240 are isolated by an EOF analysis. These are the PDO and the NPGO, and we will refer to
241 them as the leading SST modes throughout the remainder of the paper. The EOF analysis
242 is applied to unfiltered December through February (DJF) seasonal mean anomalies of
243 SST over the region 120°E-100°W, 20°N-60°N. The corresponding global spatial
244 patterns are obtained by regressing the normalized principal components (PCs) on the
245 DJF SST anomalies. Figure 2 shows these regressed fields based on 350 years of the
246 model run and 141 years (1871-2011) of the Hadley Center SST. The first EOF captures
247 the familiar horseshoe pattern of the PDO and explains 29% of the normalized variance
248 in the model and 30% in the observations out of their total variance values which are 0.36
249 and 0.21 $(°C)^2$, respectively (Figs. 2a, c).
250
251 Recently, there has been some interest in another leading mode of North Pacific SST
252 variability, including its timescale, mechanisms and its role in the Pacific interannual-
253 decadal variability (Bond et al. 2003; Di Lorenzo et al. 2008). Found here as EOF2 in the
254 model and EOF3 in the observations, it depicts a nearly north-south dipole structure,
255 which is similar to the SST pattern in Bond et al. (2003) (Victoria mode) and the North

256 Pacific Gyre Oscillation (NPGO) in Di Lorenzo et al. (2008). We note that the rank of
257 this mode appears sensitive to the observational period; while the NPGO is resolved as
258 EOF2 for the period 1950-2011, its variance is reduced over the period 1871-2011.
259
260 We focus on the EOFs for the DJF season in order to better capture the PDO-ENSO
261 relation in the model. We note that although an EOF analysis of the annual mean SST
262 yields similar patterns and variance decomposition, the simulated ENSO-PDO covariance
263 is absent in that case: the regression coefficients in the ENSO region are less than 0.05.
264 The regression values for DJF are, however, still small (~0.2) compared with those for
265 the observations (~0.6) (Fig. 2c) and we will discuss this point further in the following
266 sections.
267
268 In Figure 2, there are two major differences between the model and observations. Firstly,
269 the model overestimates the variance of both poles of the PDO mode. The negative
270 anomalies in the western part of the basin (at about 40°N) and the positive anomalies
271 over the Gulf of Alaska are nearly double that of their observational counterparts. The
272 variance is particularly large in the western north Pacific region where the influence of
273 the Kuroshio-Oyashio currents is important. The PDO pattern has potentially two centers
274 of action, one in the western basin and another in the central part of the basin, the latter
275 being related to ENSO (Deser and Blackmon 1993). In the observations, the central
276 Pacific maximum appears dominant. In the model, this distinction is less clear and
277 appears to be related to the nature of the ENSO, which has a pronounced biennial
278 spectrum (figure not shown). The dominance of the KOE variance has also been seen in

279 different versions of the NCAR Community Climate System Model (CCSM), (Kwon and
280 Deser, 2007; Deser et al. 2012) as well as in many models that participated in the
281 Intergovernmental Panel on Climate Change (IPCC) Fourth Assessment (AR4) (Furtado
282 et al. 2011).
283
284 Secondly, as mentioned before, the tropical signal is weak in the model. Compared to a
285 broad ENSO-like pattern in the eastern Pacific found in the observations, the model
286 shows weaker signals slightly shifted to the west. The apparent weak relation with ENSO
287 is evident in the temporal correlation between PC1 and Nino3: 0.17 in the seasonal DJF
288 unsmoothed data and 0.34 when both time series are subjected to a 5-year running mean.
289 (The Nino3 index is defined as the SST anomalies averaged over 150°W-90°W, 5°S-
290 5°N). The corresponding value in the observations is 0.57 in the unfiltered data for the
291 period 1870-2011. Reasons for this general weakness of the ENSO-PDO relationship will
292 be examined in Section 3.3.
293
294 The power spectrum of the PDO for the entire simulation (350 years) has three peaks
295 around 31, 18 and 7 years respectively, which are not statistically significant at the 10%
296 level (figure not shown). Similarly, the NPGO has spectral peaks around 15 and 7 years
297 that are not statistically significant (figure not shown). The lack of significance is even
298 more evident when spectral power is computed independently for two or more segments
299 of the data and averaged. What is shown in Fig. 3 is such an average over two 141-year
300 segments, which shows a red spectrum with small increases in power near 28 and the 9-5
301 year band. The results are similar when averaging is done over three 100-year segments.

302 Notice that no distinct peaks are present either in the PDO or in the NPGO, which is not
303 inconsistent with the observations (Fig. 4) although questions remain about the accuracy
304 of the observational records.
305
306 This is different from the finding of Kwon and Deser (2007), where they found a
307 statistically significant 16-year spectral peak in a 650-year long simulation of the
308 CCSM2. A distinct spectral peak implies a preferred oscillation that could arise from
309 either atmosphere-ocean feedback or from resonance. In CCSM2, the basin-wide wind
310 stress curl forcing excites Rossby waves in the central Pacific and results in a delayed
311 response in the surface temperature in the western boundary that in turn propagates
312 eastward. These processes, wave propagation and advection combined, form an 8-year
313 half cycle and closure of this cycle depends whether and how the atmosphere responds to
314 the KOE SST. In CCSM2, the atmospheric response (in wind stress curl) to KOE SST is
315 about 35% weaker than the original forcing; yet, the response is of opposite sign to the
316 forcing, a necessary condition for establishing a coupled oscillation with a 16-year cycle.
317 The fact that there is no distinct spectral peak in the GEOS-5 diminishes the prospects of
318 a coupled self-sustained oscillation in this model. But that does not rule out the Rossby
319 wave mechanism in this model – for example if the atmospheric response to the KOE
320 SST anomalies is insufficient to generate a closed loop. Wind stress curl forced Rossby
321 waves may still be present and influence the KOE SST anomalies and therefore the
322 objectives of the study remain valid.
323

In the remaining sections of the paper, we mainly focus on the model data. The main reason for this is that the accuracy of the observational records before 1950 may be questionable and statistical calculations (such as regression) may not provide a benchmark to make meaningful comparisons against the model. Instead, the understanding gained from case studies such as the decadal shift of the 1976 (a phase change where data are more reliable) may be more useful and would help us to better evaluate the model. The wind-stress curl forced Rossby waves is a mechanism proposed to explain the 1976 phase shift (Deser et al. 1999; Seager et al. 2001) and we will take this as an observational benchmark in this study.

3.3. Tropical connection

As mentioned before, the observed relatively strong relation between the PDO and ENSO is not captured in the model. The simultaneous correlation between the PC1 of SST and the Nino3 index is 0.17 in the unsmoothed DJF seasonal data in contrast to 0.45 in the observations. We speculate that the ENSO-induced SST fluctuations do not project onto the PDO in the simulation. A mechanism by which ENSO can generate low frequency fluctuations involves persistence of temperature anomalies in the mixed layer for a few years aided by 'reemergence'. This may operate in nature where the ocean has a chance to retain an initial anomaly for 4-5 years between two consecutive ENSO events. In the model, however, the time scale of ENSO is too short (dominant period of 2-3 years) such that a positive ENSO event in one winter is often immediately followed by a negative

346 event in the next winter and therefore is unlikely to force low frequency variability in the
347 North Pacific.
348
349 The ENSO-forced signals in the North Pacific can also be examined in terms of Nino3-
350 based monthly lagged composites of SST and SLP (Fig. 5). A warm phase is defined
351 when DJF Nino3 exceeds +1 standard deviation and vice versa. The circulation response
352 consisting of negative SLP anomalies during the warm phase and positive SLP anomalies
353 during the cold phase is in agreement with observations. Several studies have examined
354 the effect of this atmospheric teleconnection on the North Pacific SST (see, Alexander et
355 al. 2002 for a review). During a warm ENSO phase, a negative SLP anomaly in the North
356 Pacific results in anomalous northwesterlies and cold dry air advection to the
357 northwestern Pacific, anomalous southerlies and warm moist air advection to the West
358 coast of the North America and anomalous westerlies and increased total westerly winds
359 in the central Pacific. The resulting surface heat flux and Ekman advection anomalies
360 cool the ocean west of 150°W and warm the ocean on the eastern side. During a cold
361 ENSO phase, these anomalies are reversed. Unlike the response during warm ENSO
362 events, the response in SST for cold ENSO events is weak and incoherent in the model.
363 In the cold composites, negative SST values occur in the North Pacific as late as
364 November, suggesting that negative anomalies from a previous warm ENSO persist into
365 the following fall. This provides an unfavorable condition for circulation anomalies
366 associated with a cold ENSO phase to generate warm SST anomalies. This problem is
367 clearer when composites are extended into the preceding fall and the following summer
368 (figure not shown). During summer, the tropical Pacific reverses sign abruptly while the

369 extra-tropical SST anomalies retain the sign gained in the previous winter. This results in
370 an erroneous Pacific SST pattern consisting of a cold tropics and subtropics or a warm
371 tropics and subtropics. Interestingly, this behavior is obvious only in the cold composites.
372 Studies that examined the asymmetric response to ENSO show that, it is the cold events
373 that force larger circulation and SST anomalies than warm events (Hoerling et al. 1997;
374 An et al. 2007), while our model composites show the opposite. The reasons for this
375 asymmetry are not immediately clear from the present analysis. Nevertheless, the
376 composite analysis verifies our earlier conclusion in Section 3.2 that the tropically forced
377 SST anomalies in the model occur in the central Pacific slightly south of 40°N, which is
378 in agreement with observations, while the PDO variance (see, Fig. 2) is maximum over
379 the western basin. We summarize therefore that the influence of ENSO may in fact be
380 contributing to interannual fluctuations in North Pacific SST, but not necessarily
381 projected onto the decadal timescales studied here.
382
383 **3.4. Extra-tropical atmospheric forcing and feedback**
384
385 We now move on to looking more directly at the role of extra-tropical atmospheric
386 forcing of the PDO. Several studies have pointed out the correlation between Aleutian
387 low variability (often depicted by the North Pacific Index or NPI) and the PDO (Deser et
388 al. 1999; Kwon and Deser, 2007; Schneider and Cornuelle, 2005)). The NPI is an area-
389 average of SLP anomalies over the region 30°N-65°N, 160°E-140°W as defined in
390 Trenberth and Hurrell (1994), and captures a monopole pattern similar to the first EOF of
391 winter SLP anomalies. However, we know that the influence of ENSO on the Aleutian

low variability is not negligible as the two indices (NPI and Nino3) are correlated at 0.5, indicating that the ENSO accounts for about 25% of the Aleutian low variance. Additionally, the ENSO composites of SLP (Fig. 5) indicate an atmospheric response over the Aleutian low region. Therefore, the Aleutian low variability is likely a combination of internal atmospheric and the ENSO-forced variability and in the following analysis we attempt to separate these two components by linear regression.

a) AR1 forecast:

We will first examine the influence of NPI by adopting a simple AR1 model with an additional forcing term to represent the NPI, following Newman et al. (2003). Accordingly, the PDO is represented as follows:

$$P(t) = \propto P(t-1) + \beta S(t) + \eta(t)\,, \qquad (1)$$

where $P(t)$ is the PDO forecast at time t, $P(t-1)$ is the PDO one time step earlier, S is an index to represent external forcing (e.g., NPI) and η is an uncorrelated noise term. The coefficients β and $\propto$ are obtained, respectively, by regressing the PDO on the NPI time series and then auto-regressing the residual PDO times series (that is obtained after removing the NPI) with a lag of one year. Forecasts are made for one time step (or 1 year) at a time and then reinitialized and run for the next time step and so on. To separate the ENSO-forced part of the NPI, a revised NPI (NPI*) is defined, which is obtained by removing the ENSO signal by linear regression with the Nino3. The NPI* is an approximation to the inherent (internal) extra-tropical atmospheric variability. We make two forecasts, first with the total NPI, and then with the NPI*.

414 Figure 6 shows scatter plots of the PDO versus the NPI and the NPI* (Figs 6a,b) and the
415 AR1 forecasts of the PDO when run with NPI and NPI* (Figs. 6c,d). The correlation
416 between the PDO and the NPI (i.e., β in (1)) remains unchanged whether or not ENSO is
417 present, and therefore, the skill of the forecast. This suggests that the ENSO-forced part
418 of the NPI is not the key forcing of the PDO and that the ENSO-forcing is likely limited
419 to the high frequency variability (1-2 years) of the NPI. These results are again consistent
420 with our previous finding that the role of the ENSO on the PDO is negligible in this
421 model. This finding is however different from those based on observations. For example,
422 Schneider and Cornuelle (2005) found that by removing ENSO from observed North
423 Pacific SLP anomalies, the skill of the AR1 reconstruction of the PDO was reduced from
424 ~0.8 to ~0.55. They identified a region, where intrinsic midlatitude SLP variability is
425 important for the PDO reconstruction, which is approximately collocated with the NPI
426 region of Trenberth and Hurrell (1994), used in this study.
427
428 b) Atmospheric-Ocean feedback
429 In view of the simultaneous covariance between the NPI/Aleutian low and the PDO, we
430 next examine lead/lag relationships between the atmosphere and SST in order to
431 understand forcing and response between atmosphere and SST. We remind the reader
432 that the original Latif-Barnett hypothesis (Latif and Barnett, 1994) called for an oceanic
433 origin of the SST in which case one would expect NPI anomalies to lag the PDO. There
434 is however a general agreement in recent studies that the NPI leads the PDO (e.g., Kwon
435 and Deser, 2007; Deser et al. 2012). Another recent finding is that the second mode of the
436 SST (NPGO) is correlated with the North Pacific Oscillation (NPO) (Chhak et al. 2009).

437 The NPO is an SLP pattern identified by Walker and Bliss (1932) that has a meridional
438 dipole structure, with opposite signed anomalies in Alaska and Hawaii.
439
440 We first isolate the Aleutian low and NPO patterns by computing EOFs of DJF SLP and
441 wind stress curl over the region 120°E-100°W, 20°N-60°N (Fig. 7). Here, instead of
442 using the NPI index, we use the EOF analysis to identify the Aleutian low since this
443 enables a cleaner separation of the Aleutian low and the NPO. The EOFs of the SLP and
444 the wind stress curl essentially capture the same modes: the temporal correlation between
445 the corresponding PCs are greater than 0.9. The first mode (Figs. 7a,c) shows the
446 Aleutian low and its signature in wind stress curl, the temporal variability of which is
447 essentially the NPI: PC1 of the wind stress curl is correlated with the NPI with a value of
448 0.97. The second mode captures the characteristic meridional dipole structure of the
449 NPO. Consistent with internally forced midlatitude atmospheric behavior, (e.g., Wallace
450 and Gutzler 1981; Esbensen 1984) the temporal variability of these modes at interannual
451 time scales shows a white spectrum without any preferred periodicity (figure not shown).
452 In the following analyses, we will use PCs 1 and 2 of the wind stress curl to represent the
453 Aleutian low and NPO, respectively.
454
455 Figure 8 shows lead/lag correlations between the PCs of the wind stress curl and the SST.
456 All time series are subjected to a 6-year low-pass filter to better capture decadal-scale
457 variability. First of all, considering the relation between the Aleutian low and the PDO,
458 the correlation is at maximum (~0.7) when the atmospheric mode leads the SST mode by
459 1 year, suggesting an atmospheric forcing of the SST (Fig. 8, bottom panel). Similarly,

460 the NPO appears to force the NPGO with a maximum correlation of ~0.4 at lag -1. The 1-
461 year lag between NPO and the NPGO is in agreement with previous studies (Chhak et al.
462 2009). In the case of the PDO, the 1-year lag is too short to invoke the wind stress curl
463 induced Rossby wave mechanism, in which Rossby wave propagation from the central
464 Pacific to the western boundary sets the delay time between the Aleutian low and the
465 PDO SST anomaly. The short time lag obtained here is not in agreement with the results
466 based on CCSM (Kwon and Deser, 2007; Deser et al. 2012), where lags of 2-4 years
467 were found that are consistent with a Rossby wave mechanism. Rossby wave phase
468 speed estimates for 40°N suggest 3-5 years are needed to propagate from 160°E to the
469 western boundary (Chelton and Schlax, 1996).
470
471 Secondly, we notice that there are weak correlations between the PDO and the NPGO
472 when the PDO leads the NPGO by 3 years and similarly between the Aleutian low and
473 the NPO when the former leads by 3 years (Fig. 8, top panel). These values are about 0.4
474 and 0.2, respectively and they are marginally significant at the 5% level. A similar weak
475 relationship (statistically significant at 5% significance level) can be found between the
476 PDO and the NPO when the former leads the latter by 2 years, suggesting that the
477 atmospheric response of the PDO projects onto the NPO. In view of the above
478 correlations, we propose a connection between the PDO and the NPGO, which involves
479 the following processes in the order they are listed: 1) an initial Aleutian low anomaly
480 forces the PDO, 2) the atmosphere responds to the PDO which results in an NPO-like
481 pattern, and 3) the NPO forces the NPGO SST pattern.
482

To further address the atmospheric forcing and response, lead lag regression and correlations are computed for SLP and wind stress curl data with respect to the PDO and the NPGO (Figs. 9, 10). Regression with SST is shown (left column in Figs 9, 10) to understand the progression of the EOF patterns. In the regressions with atmospheric variables, a positive lag means the atmosphere lags the ocean and therefore the regressed fields represent an atmospheric response and similarly a negative lag suggests atmospheric forcing. Only lags from -2 to +3 years are examined, as they appear relevant based on Fig. 8. In the case of PDO (Fig. 9), lags -2 to 0 show SLP and wind stress curl patterns that represent the Aleutian low, similar to the EOFs 1 in Fig. 7. The atmospheric response to the PDO (lags +1 to 3) is of opposite sign to the forcing, and forms over the western boundary, expanding eastward, south of 40°N. Although the response is of opposite sign to the forcing, it does not develop into the monopole structure of the Aleutian low, rather it bears similarities to the NPO pattern (see, Figs, 7c,d). Figure 10 shows that an NPO-like structure in SLP and wind stress curl leads the NPGO, as one would expect from the correlation curve in Fig. 8. Also, notice that at lag -2 the SST and SLP patterns are similar to the PDO where the SST has maximum amplitude at the western boundary at 40°N, and the SLP has the Aleutian low structure. This is again consistent with Fig. 8, where we showed that the PDO leads the NPGO.

In summary, the lead/lag regression analysis conveys the following. 1) It is unlikely that the atmospheric response to the PDO matures into the original forcing pattern of the Aleutian low. Instead, the response appears to project onto a meridional dipole in SLP, which is similar to the NPO pattern. 2) And therefore, the atmospheric response to the

PDO may help force the NPGO. 3) The atmospheric response is generally weak – a rough estimate from the regression analysis is that the response is 25% of the forcing.

c) Oceanic response to the Aleutian low

A key question now is how the SST anomalies are generated, i.e., whether they are due to surface heat fluxes and Ekman layer advection, processes that are fast and local, or by wind-stress curl induced Rossby waves (e.g., Deser et al. 1999; Seager et al. 2001; Kwon and Deser, 2007), a delayed response to the Aleutian low in the KOE region, which can take 3-5 years to generate SST anomalies in the KOE region. To separate these processes, we consider the following familiar approximation for the mixed layer heat budget (see, review by Frankignoul 1985)

$$\frac{\partial T}{\partial t} = -\frac{Q}{\rho_0 C_p h} - \left(\boldsymbol{V}_E + \boldsymbol{V}_g\right) \cdot \boldsymbol{\nabla} T + R \qquad (2)$$

where T is the mixed layer temperature or equivalently SST, Q is the net surface heat flux, ρ_0 is the density of sea water (1025 kgm^{-3}), C_p is the specific heat capacity of sea water (3986 Jkg^{-1}K^{-1}), h is the mixed layer depth and $\boldsymbol{V}_E$ and $\boldsymbol{V}_g$ are horizontal vectors of Ekman and geostrophic velocity, respectively. The rest of the terms form the residual, R that include diffusion and entrainment. The Ekman transport is computed from wind stress as, $\boldsymbol{V_E} = \boldsymbol{k} \times \boldsymbol{\tau} / \rho_0 f h$, and the surface geostrophic velocity is obtained from sea surface height as, $\boldsymbol{V_g} = -\boldsymbol{k} \times \boldsymbol{\nabla} \eta (g/f)$, where $\boldsymbol{\tau}$ is the surface horizontal wind stress vector, η is the sea surface height and g and f are gravity and Coriolis parameter, respectively. Total fields of surface currents are obtained from the DJF mean wind stress and sea surface height from which DJF anomalies are calculated by subtracting the climatology. The mixed layer depth in the Ekman current calculation is the climatological

527 mean 2D field, which ranges from 80-140m west of dateline between 30°N-50°N and is
528 less than or equal to 60m over the rest of the basin.
529
530 We will examine regressed fields of net heat flux, horizontal Ekman and geostrophic
531 temperature advection (from (2)) with respect to an index of the PDO. It is not yet clear
532 whether the NPGO is completely independent of the PDO and therefore, in this section
533 we focus only on the PDO and its association with the KOE SST anomalies. For this
534 purpose, we define an area-averaged SST index over the KOE region (140°E-180°E,
535 35°N-45°N) (KOE index, hereafter), instead of using the PC time series of the PDO.
536
537 Figure 11 shows regressed fields of the net surface heat flux with respect to the KOE
538 index. The atmosphere leads or is simultaneous with the SST at negative and zero lags.
539 At negative or zero lags, a positive regression coefficient implies either 1) heat flux is
540 positive (into the ocean) and consequently SST increases or 2) heat flux is negative (into
541 the atmosphere) and ocean surface cools in response. Positive values south of the KOE
542 region and over the central parts of the basin, therefore suggests that those are the regions
543 where the surface heat flux forces SST anomalies. On the other hand, negative values in
544 the KOE region (40°N-50°N) implies that heat flux is out of the ocean as SST increases,
545 suggesting that oceanic processes are important in controlling the SST, and surface heat
546 flux works to only damp the SST.
547 Figure 12 shows the regressed fields of anomalous Ekman and geostrophic advection of
548 temperature with respect to the KOE index. Anomalous advection terms are computed
549 from (2) by subtracting the climatological mean to obtain $\overline{\boldsymbol{V}} \cdot \boldsymbol{\nabla} T'$, $\mathbf{V}' \cdot \boldsymbol{\nabla} \overline{T}$, and $\boldsymbol{V}' \cdot \boldsymbol{\nabla} T'$,

550 which are advection of anomalous temperature by mean currents, advection of mean
551 temperature by anomalous currents and advection of anomalous temperature by
552 anomalous currents, where $\boldsymbol{V} = (\boldsymbol{V}_E, \boldsymbol{V}_g)$. The 'overbar' denotes climatology and 'prime'
553 denotes deviations from climatology. The sum of the three terms forms the total
554 anomalous advection. In Fig. 12, negative values denote areas where heat transport
555 contributes to a positive KOE index. The Ekman temperature advection terms appear to
556 determine the SST over most of the PDO pattern, especially east of 160°E. This is clear
557 in panel (b) that shows the product of the anomalous Ekman current and the mean
558 temperature gradient. The panel (a) represents advection of Ekman current across
559 anomalous temperature gradients, which is dominant west of 160°E and between 38°N-
560 42°N. Here, the anomalous temperature gradient is not necessarily only due to Ekman
561 transport; it could be due to surface heat fluxes, geostrophic transport or other mixed
562 layer processes that are not considered here. From Fig. 11, we see that surface heat flux
563 term is important in the western boundary in areas south of 40°N, which partially
564 overlaps our area of focus in panel (a). The anomalous geostrophic advection (panel h),
565 on the other hand, is limited to a narrow strip above 42°N, west of 160°E, and it is
566 unlikely a major contributor for panel (a). Therefore, the anomalous temperature
567 gradients between 38°N-42°N that contribute to the term in panel (a), is unlikely due to
568 geostrophic transport. The surface geostrophic advection represents the delayed
569 response at the KOE, which can be manifested by Rossby waves from the east either
570 resulting in the strengthening/weakening of the gyre (Latif and Barnett 1994) or by the
571 meridional shift at the confluence of the subtropical and sub polar gyres (Seager et al.
572 2001). Figure 12 indicates that in GEOS-5, the Ekman transport dominates over the slow

573 geostrophic advection. This is consistent with the short lag (1 year as opposed to 3-4
574 years) between the Aleutian low and the PDO, shown in Fig. 8.
575
576 In agreement with previous studies (Seager et al. 2001; Kwon and Deser 2007, among
577 others), we find that the geostrophic anomalies are of the same sign as the Ekman
578 anomalies. The phase reversal of the KOE SST, therefore, has its origins in the
579 atmosphere, as proposed by recent studies as opposed to the ocean, which was the earlier
580 proposal by Latif and Barnett (1994). The lead lag regressions in Fig. 9 indicate that the
581 atmospheric response to the SST is rather weak and does not project on to the Aleutian
582 low. This leaves us with the possibility that the PDO in this model is mostly an oceanic
583 surface layer response to the Aleutian low and is unlikely a coupled ocean-atmosphere
584 oscillation.
585
586 **4. Summary and discussion**
587 In this study, we examined the characteristics and mechanisms of Pacific decadal
588 variability in a 350-year long simulation of the GEOS-5 atmosphere-ocean general
589 circulation model.
590
591 The GEOS-5 simulates a realistic pattern of decadal variability characterized by a PDO-
592 like horseshoe pattern in the SST. The time series of this pattern does not have a
593 statistically significant preferred oscillation, and can instead be best characterized by a
594 red noise process. The PDO in this model is likely primarily forced by midlatitude
595 atmospheric noise and is little influenced by tropical SSTs associated with the ENSO

596 phenomenon. The lack of a substantial role of ENSO may be related to the unrealistically
597 short time scales of ENSO in the model of about 2-3 years, which is unlikely to be
598 influential on the decadal timescale of the North Pacific SST. The lack of a substantial
599 tropical connection must be a model bias since observational studies suggest ENSO as
600 one of the triggering mechanisms for the PDO (Newman et al. 2003; Schneider and
601 Cornuelle, 2005).
602
603 The Aleutian low and the associated basin-wide wind stress curl pattern are correlated
604 with the PDO at ~0.7 when the former leads the PDO by 1 year. The 1-year delay
605 suggests that the local fast response of the ocean by surface heat fluxes and Ekman
606 transport takes precedence over any delayed remote response at the KOE region. The
607 Ekman transport is dominant over most of the central and western parts of the PDO,
608 while the influence of the geostrophic transport is limited to a narrow strip at 40°N. The
609 geostrophic component is of the same sign as the Ekman component, and therefore
610 reinforces the SST anomalies set by the Ekman transport. This has been reported in many
611 previous studies (Seager et al. 2001; Schneider et al. 2002; Kwon and Deser, 2007) and it
612 undermines the earlier notion that the geostrophic adjustment at the KOE is the point of
613 origin of the phase reversal of the PDO (Latif and Barnett 1994). The role of Rossby
614 waves and delayed response at the KOE were reported to be crucial components of the
615 PDO in some model and observational studies (Deser et al. 1999; Seager et al. 2001;
616 Kwon and Deser 2007), whereas we find that the SST is largely controlled by the surface
617 layer response. It is worth noting that in this study the Ekman transport is sizable even

618 when 10-year low pass filtered wind stress data is used, suggesting that low frequency
619 variability in the Aleutian low is the key-controlling factor.
620
621 The lack of preferred periodicity implies that a coupled atmosphere-ocean oscillation is
622 unlikely an important mechanism for the PDO simulated in GEOS-5 as opposed to
623 CCSM2.0 where a statistically significant 16-year peak was found (Kwon and Deser
624 2007). This is further substantiated by the weak atmospheric feedback to the SST (only
625 25% of the initial Aleutian low forcing). Additionally, it appears that the atmospheric
626 response never matures into the monopole structure of the Aleutian low in order to set up
627 a self-sustained oscillation, instead projecting onto the second EOF of the SLP, the NPO.
628 The NPO in turn forces an SST pattern, the NPGO, which is resolved as the second EOF
629 of the SST.
630
631 In agreement with the previous studies (Chhak et al. 2009), the NPO is an atmospheric
632 forcing pattern for the NPGO. However, the PDO and the NPGO, although resolved as
633 orthogonal EOFs, are correlated at ~0.4 when the PDO leads the NPGO by 3 years. This
634 finding, along with the observation that the PDO's atmospheric response projects onto
635 the NPO, suggests a loose atmospheric link between the PDO and the NPGO. This
636 involves an initial Aleutian low anomaly and its oceanic response within 1 year as the
637 PDO, and the PDO's atmospheric response, which matures in 2-3 years, and its reflection
638 in the SST in the form of the NPGO. In this scenario, at least in some cases, one could
639 expect an NPGO pattern developing after 2-3 years of a PDO peak phase.
640

641 Previous model studies and results from model inter-comparisons suggest that a
642 somewhat realistic spatial structure of the PDO in the North Pacific is a feature
643 consistently simulated across the models (Kwon and Deser 2007; Furtado et al. 2011;
644 Deser et al 2012). This study provides an additional verification for that and complements
645 previous studies. A statistically significant correlation between the PDO and the Aleutian
646 low that underlines the atmospheric control over the North Pacific SST appears to be
647 another feature consistent among the models. Furtado et al. (2011) notes that this relation
648 is captured in the majority of the IPCC AR4 models. Many models, however, fail to
649 capture the tropical ENSO connection, overestimate the North Pacific SST variance, and
650 differ among the timescale selection. The fact that the PDO is almost entirely of
651 midlatitude origin in many models indicates a possible overestimation of midlatitude
652 atmospheric control over the decadal SST variability. The enhanced variance over the
653 northwestern Pacific would need further attention and may be related to mean biases such
654 as too shallow simulated mixed layer as noted by Thomson and Kwon (2010) in
655 CCSM3. The overestimation of the low frequency SST variance can also lead to too
656 optimistic model predictability estimates. The dominance of Ekman response over the
657 geostrophic adjustment indicates predictability of phase reversal of the PDO may be poor
658 in this model although persistence of a particular phase may provide some skill.
659

660 **Acknowledgments**
661
662 DA would like to thank Yoo-Geun Ham for helpful discussions.

References

Alexander, M., C. Deser, and M. Timlin, 1999: The reemergence of SST anomalies in the North Pacific Ocean. *J. Climate*, **12**, 2419–2433.

Alexander, M. A., I. Bladé, M. Newman, J. R. Lanzante, N-C. Lau, and J. D. Scott, 2002: The Atmospheric Bridge: The influence of ENSO teleconnections on air–sea interaction over the global oceans. *J. Climate*, **15**, 2205–2231.

Alexander, M. A. and J. D. Scott, 2008: The role of Ekman ocean heat transport in the Northern Hemisphere Response to ENSO. *J. Climate*, **21**, 5688–5707.

An, S-I, J-S. Kug, A. Timmermann, I-S. Kang, O. Timm, 2007: The influence of ENSO on the generation of decadal variability in the North Pacific*. *J. Climate*, **20**, 667–680.

Bond, N. A., J. E. Overland, M. Spillane, and P. Stabeno, 2003: Recent shifts in the state of the North Pacific. *Geophys. Res. Lett.*, **30**, 2183, doi:10.1029/2003GL018597

Bretherton, C. S., M. Widmann, V. P. Dymnikov, J. M. Wallace and I. Bladé, 1999: The effective number of spatial degrees of freedom of a time-varying field. *J. Climate*, **12**, 1990–2009.

Chhak, K. C., E. Di Lorenzo, N. Schneider, and P. F. Cummins, 2009: Forcing of low frequency ocean variability in the northeast Pacific, *J. Climate*, **22**, 1255–1276.

Chelton, D. B. and M. G. Schlax, 1996: Global observations of oceanic Rossby waves. *Science*, **272**, 234–238.

Compo, G.P., and coauthors, 2011: The Twentieth Century Reanalysis Project. *Quart. J. Roy. Meteo. Soc*., **137**, 1–28.

Deser, C., and M. L. Blackmon, 1993: Surface climate variations over the North Atlantic Ocean during winter: 1900-1989. *J. Climate*, **6**, 1743–1753.

Deser, C., M. A. Alexander, and M. S. Timlin, 1996: Upper-ocean thermal variations in the North Pacific during 1970–1991. *J. Climate*, **9**, 1840–1855.

Deser, C., M. A. Alexander, and M. S. Timlin, 1999: Evidence for a wind-driven intensification of the Kuroshio Current Extension from the 1970s to the 1980s. *J. Climate*, **12**, 1697–1706.

Deser, C., M. A. Alexander, M. S. Timlin, 2003: Understanding the persistence of sea surface temperature anomalies in midlatitudes. *J. Climate*, **16**, 57–72.

Deser, C., A. Phillips, and J. Hurrell, 2004: Pacific interdecadal climate variability: Linkages between the tropics and North Pacific during boreal winter since 1900. *J. Climate*, **17**, 3109–3124.

Deser, C., A. S. Phillips, R. A. Tomas, Y. Okumura, M. A. Alexander, A. Capotondi, J. D. Scott, Y. -O. Kwon, and M. Ohba, 2012: ENSO and Pacific Decadal Variability in Community Climate System Model Version 4. *J. Climate*, **25**, 2622–2651

Di Lorenzo, E., and Coauthors, 2008: North Pacific Gyre Oscillation links ocean climate and ecosystem change. *Geophys. Res. Lett*., **35**, L08607, doi:10.1029/2007GL032838.

Duchon, C. E., 1979: Lanczos filtering in one and two dimensions. *J. Appl. Meteor.,* **18**, 1016–1022.

Esbensen, S. K., 1984: A comparison of intermonthly and inter-annual teleconnections in the 700 mb geopotential height field during Northern Hemisphere winter. *Mon. Wea. Rev*., **112**, 2016–2032

Frankignoul, C, 1985: Sea surface temperature anomalies, planetary waves and air-sea feedback in the middle latitudes, *Rev*. *of Geophysics*., **23**, 357–390.

Frankignoul, C., P. Muller, and E. Zorita, 1997: A simple model of the decadal response of the ocean to stochastic wind forcing. *J. Phys. Oceanogr*., **27**, 1533–1546.

Furtado, J. C., E. Di Lorenzo, N. Schneider, and N. A., Bond, 2011: North Pacific decadal variability and climate change in the IPCC AR4 Models. *J. Climate*, **24**, 3049–3067.

Griffies, S. M., and Coauthors, 2005: Formulation of an ocean model for global climate simulations. *Ocean Sci*, **1**, 45-79, doi:10.5194/os-1-45-2005

Griffies, S. M., A. Biastoch, C. Bning, F. Bryan, G. Danabasoglu, E. P. Chassignet, M. H. England, R. Gerdes, H. Haak, R. W. Hallberg, W. Hazeleger, J. Jungclaus, W. G. Large, G. Madec, A. Pirani, B. L. Samuels, M. Scheinert, A. S. Gupta, C. A. Severijns, H. L. Simmons, A. M. Treguier, M. Winton, S. Yeager, and J. Yin, 2009: Coordinated ocean-ice reference experiments (COREs). *Ocean Modelling*, **26**, 1–46, doi:10.1016/j.ocemod.2008.08.007.

Hasselmann, K., 1976: Stochastic climate models. Part I: Theory. *Tellus*, **28**, 473–485.

Helfand and S. D. Schubert, 1995: Climatology of the simulated Great Plains low-level jet and its contribution to the continental moisture budget of the United States. *J. Climate,* **8,** 784–806.

754 Hoerling, M. P., A. Kumar, M. Zhong, 1997: El Niño, La Niña, and the nonlinearity of
755 their teleconnections. *J. Climate*, **10**, 1769–1786.
756
757 Hunke, E.C., and W.H. Lipscomb, 2008: CICE: The Los Alamos Sea Ice Model,
758 Documentation and Software User's Manual, Version 4.0. *Tech. Rep*. LA-CC-06-
759 012, Los Alamos National Laboratory, Los Alamos, NM. [Available online at
760 http://climate.lanl.gov/Models/CICE].
761
762 Jin, F.-F., 1997: A theory of interdecadal climate variability of the North Pacific ocean–
763 atmosphere system. *J. Climate*, **10**, 1821–1834.
764
765 Koster, R. D., M. J. Suarez, A. Ducharne, M. Stieglitz, and P. Kumar, 2000: A
766 catchment-based approach to modeling land surface processes in a GCM, Part 1,
767 Model structure. *J. Geophys. Res*., **105**, 24809–24822.
768
769 Kwon, Y.-O., and C. Deser, 2007: North Pacific decadal variability in the Community
770 Climate System Model, version 2. *J. Climate*, **20**, 2416–2433.
771
772 Latif, M., and T. P. Barnett, 1994: Causes of decadal climate variability over the North
773 Pacific and North America. *Science*, **266**, 634–637.
774
775 Levitus, S., R. Burgett, and T. P., Boyer, 1994a: World Ocean Atlas 1994, Volume 3:
776 Salinity. *NOAA Atlas* NESDIS 3. US Government Printing Office: Washington,
777 DC.
778
779 Levitus, S., and T. P. Boyer, 1994b: World Ocean Atlas 1994: Volume 4: Temperature.
780 *NOAA Atlas* NESDIS 4. US Government Printing Office: Washington, DC.
781
782 Liu, Z., 2012: Dynamics of interdecadal climate variability: A historical perspective. *J.*
783 *Climate*, **25**, 1963–1995.
784
785 Lock, A. P., A. R. Brown, M. R. Bush, G. M. Martin, and R. N. B. Smith, 2000: A new
786 boundary layer mixing scheme. Part I: Scheme description and single-column
787 model tests. *Mon. Wea. Rev*., **138**, 3187–3199.
788
789 Louis, J. and J. Geleyn, 1982: A short history of the PBL parameterization at ECMWF.
790 *Proc. ECMWF Workshop on Planetary Boundary Layer Parameterization*,
791 Reading, England.
792
793 Mantua, N. J., S. R. Hare, Y. Zhang, J. M. Wallace, and R. C. Francis, 1997: A Pacific
794 interdecadal climate oscillation with impacts on salmon production. *Bull. Amer.*
795 *Meteor. Soc*., **78**, 1069–1079.
796
797 Miller, A. J., D. R. Cayan and W. B. White, 1998: A westward-intensified decadal
798 change in the North Pacific thermocline and gyre-scale circulation. *J. Climate*, **11**,
799 3112–3127.
800

Miller, A. J., and N. Schneider, 2000: Interdecadal climate regime dynamics in the North Pacific Ocean: Theories, observations and ecosystem impacts. *Progr. Oceanogr.*, **47**, 355–379.

Molod, A., L. Takacs, M. Suarez, J. Bacmeister, I.-S. Song, and A. Eichmann, 2012: The GEOS-5 Atmospheric General Circulation Model: Mean climate and development from MERRA to Fortuna. *Technical Report Series on Global Modeling and Data Assimilation*, 28.

Moorthi, S., and M. J. Suarez, 1992: Relaxed Arakawa–Schubert: A parameterization of moist convection for general circulation models. *Mon. Wea. Rev.,* **120,** 978–1002.

Newman, M., G. P. Compo, and M. A. Alexander, 2003: ENSO-forced variability of the Pacific decadal oscillation. *J. Climate*, **16**, 3853–3857.

Qiu, B., 2003: Kuroshio Extension Variability and Forcing of the Pacific Decadal Oscillations: Responses and Potential Feedback. *J. Phys. Oceanogr.*, **33**, 2465–2482.

Rayner, N. A.; D. E. Parker, E. B. Horton, C. K. Folland, L. V. Alexander, D. P. Rowell E. C. Kent, and A. Kaplan, 2003: Global analyses of sea surface temperature, sea ice, and night marine air temperature since the late nineteenth century *J. Geophys. Res*., **108**, 4407 doi:10.1029/2002JD002670

Rienecker, M. M., and Coauthors, 2008: The GEOS-5 Data Assimilation System - Documentation of Versions 5.0.1, 5.1.0, and 5.2.0, *NASA Technical Report Series on Global Modeling and Data Assimilation*, Vol. **27**, 101 pp.

Saravanan, R., and J. C. McWilliams, 1997: Stochasticity and spatial resonance in interdecadal climate fluctuations. *J. Climate*, **10**, 2299–2320.

Schneider, N., A. J., Miller, and D. W., Pierce, 2002: Anatomy of North Pacific Decadal variability. *J. Climate*, **15**, 586–605.

Schneider, N., B. D. Cornuelle, 2005: The forcing of the Pacific Decadal Oscillation. *J. Climate*, **18**, 4355–4373.

Seager, R., Y. Kushnir, N. H. Naik, M. A. Cane, and J. Miller, 2001: Wind-driven shifts in the latitude of the Kuroshio–Oyashio Extension and generation of SST anomalies on decadal time scales. *J. Climate*, **14**, 4149–4165.

Sun, D-Z., J., Fasullo, T., Zhang, and A., Roubicek, 2003: On the radiative and dynamical feedbacks over the equatorial Pacific cold tongue. *J. Climate*, **16**, 2425–2432.

Thompson, L. A., Y-O. Kwon, 2010: An enhancement of low-frequency variability in the Kuroshio–Oyashio Extension in CCSM3 owing to ocean model biases. *J. Climate*, **23**, 6221–6233.

Trenberth, K.E., J.W. Hurrell, 1994. Decadal atmosphere-ocean variations in the Pacific. *Climate Dyn*., **9**, 303–319.

Vernieres, G., M. Rienecker, R. Kovach, and C. Keppenne, 2012: The GEOS-iODAS: Description and Evaluation. *NASA Technical Report Series on Global Modeling and Data Assimilation, NASA TM—2012-104606*, Vol. **30**, 61 pp.

Vikhliaev, Y., M. Suarez, A. Molod, B. Zhao, M. Rienecker and S. Schubert, 2011: Evaluation of the short-term climate variability in GEOS-5 AOGCM simulations. *WCRP Open Science Conference*, Denver, CO. [Available online at http://conference2011.wcrp-climate.org/posters/C34/C34_Vikhliaev_W179B.pdf]

Vimont, D., 2005: The contribution of the interannual ENSO cycle to the spatial pattern of decadal ENSO-like variability. *J. Climate*, **18**, 2080–2092.

Walker, G., and E. Bliss, 1932:World Weather V, *Mem. R. Meteorol. Soc*., **4**, 53–84.

Wallace, J. M., and D. S. Gutzler, 1981: Teleconnections in the geopotential height field during the Northern Hemisphere winter. *Mon. Wea. Rev*., **109**, 784–812

Zhang, Y., J. M. Wallace, and D. S. Battisti, 1997: ENSO-like interdecadal variability: 1900–93. *J. Climate*, **10**, 1004–1020.

Figure captions

Figure 1. The (a) DJF seasonal climatological SST (°C) based on 350 years of model simulation and (b) difference between model and Hadley Centre SST observation (1870-2011). The variance of DJF SST anomalies ($°C^2$) for (c) model simulation (350 years) and (d) Hadley Centre SST (1870-2011).

Figure 2. Spatial pattern of first EOFs 1 and 2 (a, b) in the model and EOFs 1 and 3 (c, d) in observations based on PC-SST regression (°C per standard deviation of the PC). The EOF is computed from de-trended unfiltered DJF seasonal SST anomalies over the region 120°E-100°W, 20°N-60°N. The corresponding PCs (grey bars) and their 5-year running means (e, f) for the model and (g, h) and observations in standard deviation units. Observation is from the Hadley Centre SST (1870-2010). Percentage of explained variance (noted in plot labels) is based on total variance values of 0.36 for the model and 0.21 for the observation.

Figure 3. Power spectrum of the (a) PC1 and (b) PC2 of the SST EOFs (thick black line). An average spectrum of 2 141-year long segments from the 350-year long simulation is plotted. Thin solid line is spectrum of best-fit AR1 process and dotted line is associated 10% confidence level.

Figure 4. Power spectrum of the (a) PC1 and (b) PC3 of EOF modes of observational SST for the period 1817-2011. Thin solid line is spectrum of best-fit AR1 process and dotted line is associated 10% confidence level.

Figure 5. Cold and warm composites of monthly SST (shading) and SLP (contour) anomalies based on DJF Nino3 index based on (columns 1 and 3, from left) model simulation (350 years) and (columns 2 and 4 from left) for Hadley Centre SST and NOAA 20^{th} Century Reanalysis SLP (1871-2010). Months are noted in panel labels and the numbers in bracket denote number of months leading or lagging from January. Contour levels are +(-) 4, 3, 2, 1.5, 1, 0.5 and 0. Dotted lines represent negative contours.

Figure 6. Scatter plot of the PC1 of the DJF SST anomalies (PDO index) against (a) North Pacific Index (NPI) and (b) against the revised NPI that is obtained after removing the ENSO signal by linear regression (NPI*). The right panels show the PDO index (black curve in c, d) and their respective AR1 forecasts (red curve in c, d) (c) using the total NPI and (d) using the NPI*. Correlation coefficients between PDO and the NPI or NPI* form the β parameter for the AR1 forecasts in (c, d). All data are from the model simulation.

Figure 7. EOFs 1 and 2 of DJF (left) SLP and (right) wind stress curl anomalies for the model simulation. Percentage of variance (noted in plot labels) is based mean variance of 8.8 for SLP and 3.9E-5 for wind stress curl. The EOFs are multiplied by the standard deviation of the PCs to have units (a, b) hPa and (c,d) $Nm^{-3}10^{-7}$.

Figure 8. The (top) lead/lag correlation between the (open circle) PC1 and PC2 of SST and (closed circle) PC1 and PC2 of wind stress curl. The (bottom) Lead/lag correlation between (open circle) PC1 of SST and PC1 of wind stress curl, (closed circle) PC2 of SST and PC2 of wind stress curl and (open square) PC1 of SST and PC2 of wind stress curl. Negative lags in the top panel indicate PC1 leads PC2 and in the bottom panel atmosphere leads SST. Horizontal lines with a symbol represent 5% significance level for based on two-sided t-test. Since only positive correlation coefficients are discussed, significance level is noted only for that. All time series are 6-year low pass filtered. All data are from the model simulation.

Figure 9. Lead/Lag regressions (shading) and correlations (contours) of (column 1) SST (°C), (column 2) SLP (hPa) and (column 3) wind stress curl (10^{-8} Nm^{-3}) w.r.t the normalized PC1 of SST (i.e., PDO index). Lags are in years. Negative (positive) lag indicates PDO lags (leads) the field. All variables are from the model simulation and are 6-year low pass filtered. Hatching indicates significance at 5% level from a two-sided t-test.

Figure 10. Same as Fig. 9: but w.r.t the PC2 of the SST or the NPGO index.

Figure 11. Lead/lag regressions (shading) and correlations (contours) of the net surface heat flux (Wm^{-2} per °C) with respect to the KOE index. Positive net heat flux is directed into the ocean. Hatching indicates 5% significance level based on a two-sided t-test.

Figure 12. Simultaneous regressions (shading) and correlations (contours) of temperature advection by (left column) Ekman and (right column) geostrophic currents in the mixed layer (Wm^{-2} per °C) with respect to the KOE index. The anomalous transport is decomposed into (a, e) advection of temperature anomaly by mean currents or $\overline{\boldsymbol{V}} \cdot \boldsymbol{\nabla} T'$, (b, f) advection of mean temperature by anomalous currents or $\mathbf{V}' \cdot \boldsymbol{\nabla} \overline{T}$, (c, g) advection of temperature anomaly by anomalous currents or $\boldsymbol{V}' \cdot \boldsymbol{\nabla} T'$, and (d, h) sum of all three or total anomalous transport, where $\boldsymbol{V}$ stands for total Ekman or geostrophic velocity vector in the mixed layer. The overbar denotes climatological mean and prime denotes deviation from climatology. Hatching indicates 5% significance level.

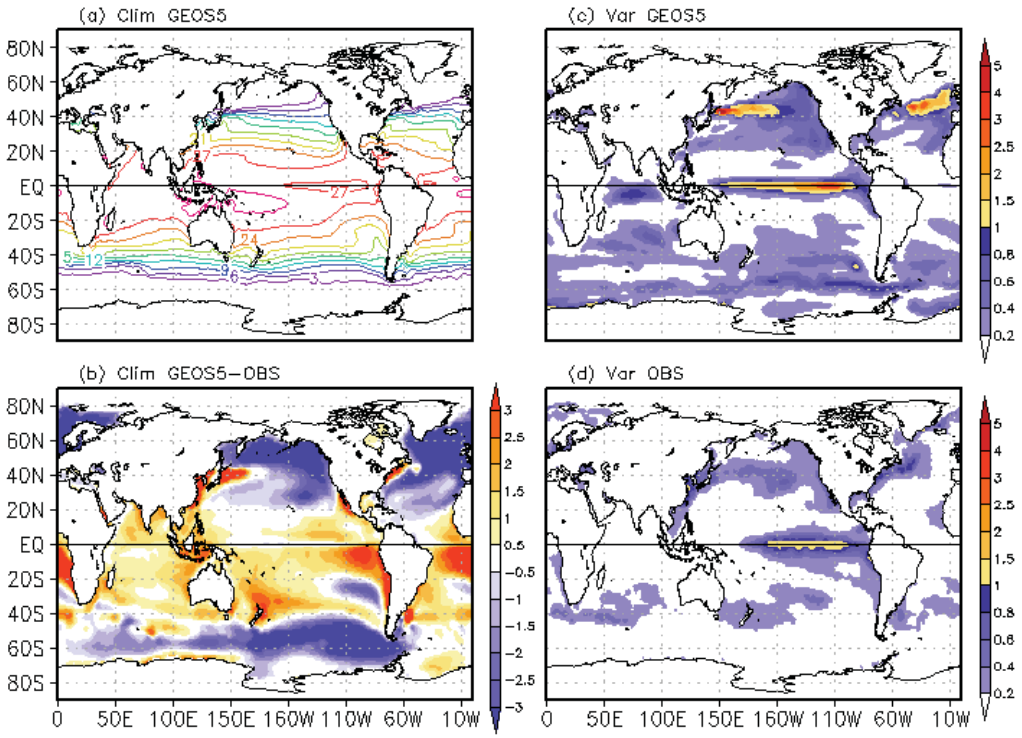

954
955 Figure 1. The (a) DJF seasonal climatological SST (°C) based on 350 years of model
956 simulation and (b) difference between model and Hadley Centre SST observation (1870-
957 2011). The variance of DJF SST anomalies ($°C^2$) for (c) model simulation (350 years)
958 and (d) Hadley Centre SST (1870-2011).
959

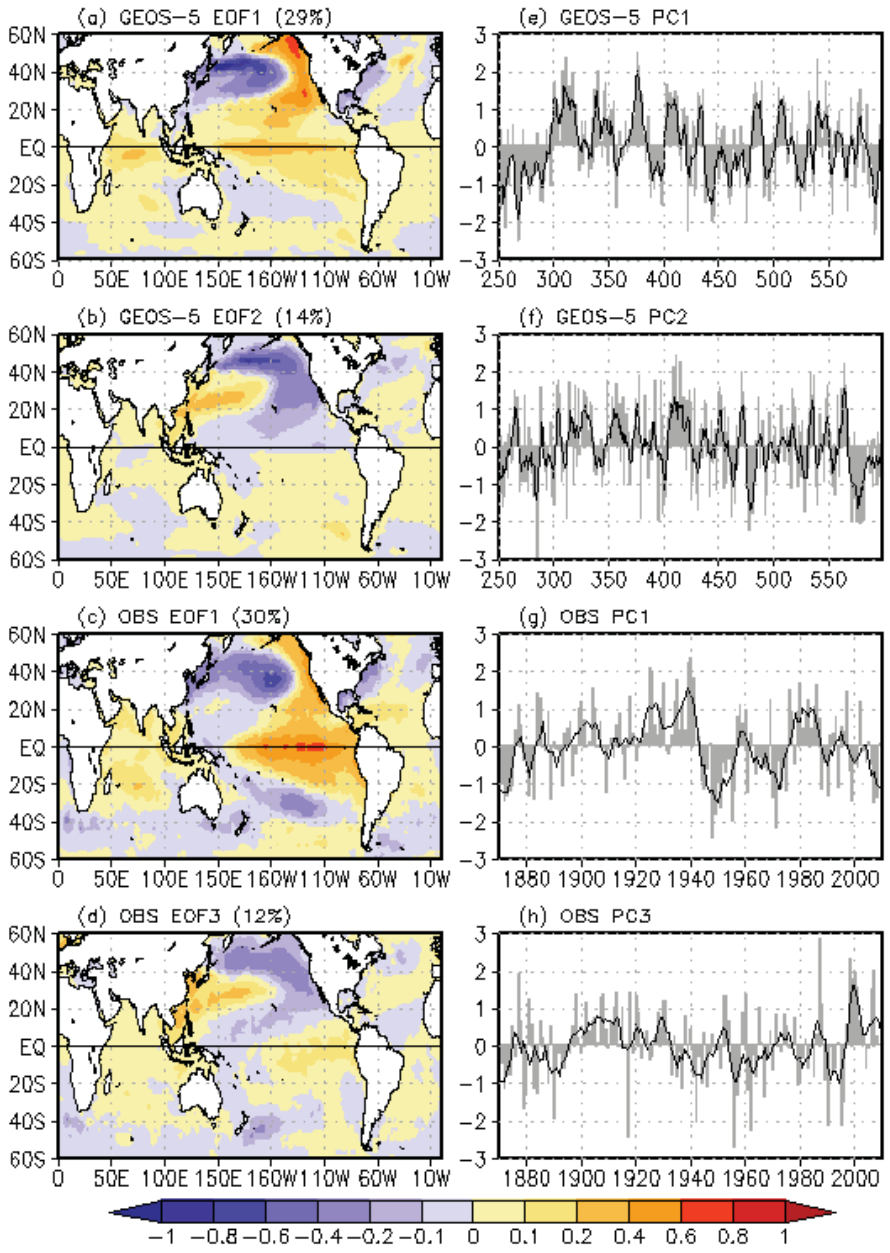

Figure 2. Spatial pattern of first EOFs 1 and 2 (a, b) in the model and EOFs 1 and 3 (c, d) in observations based on PC-SST regression (°C per standard deviation of the PC). The EOF is computed from de-trended unfiltered DJF seasonal SST anomalies over the region 120°E-100°W, 20°N-60°N. The corresponding PCs (grey bars) and their 5-year running means (e, f) for the model and (g, h) and observations in standard deviation units. Observation is from the Hadley Centre SST (1870-2010). Percentage of explained variance (noted in plot labels) is based on total variance values of 0.36 for the model and 0.21 for the observation.

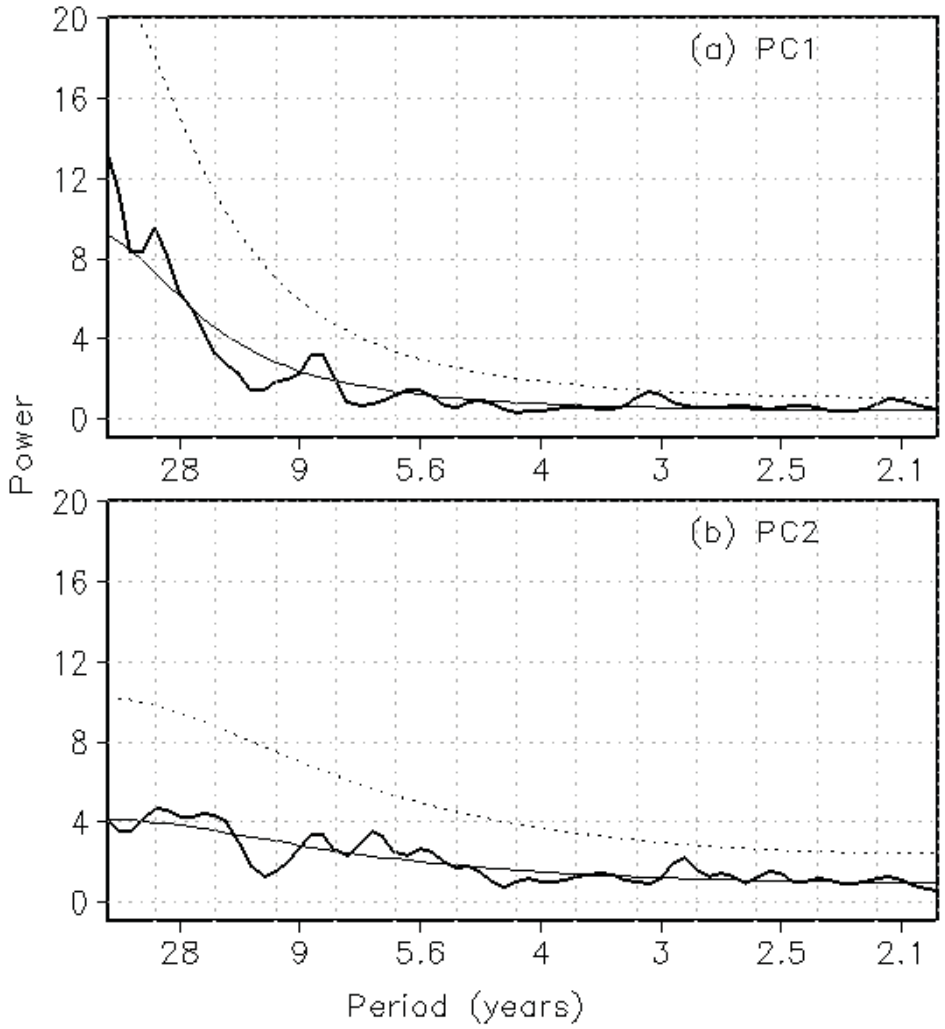

969
970 Figure 3. Power spectrum of the (a) PC1 and (b) PC2 of the SST EOFs (thick black line).
971 An average spectrum of 2 141-year long segments from the 350-year long simulation is
972 plotted. Thin solid line is spectrum of best-fit AR1 process and dotted line is associated
973 10% confidence level.
974
975

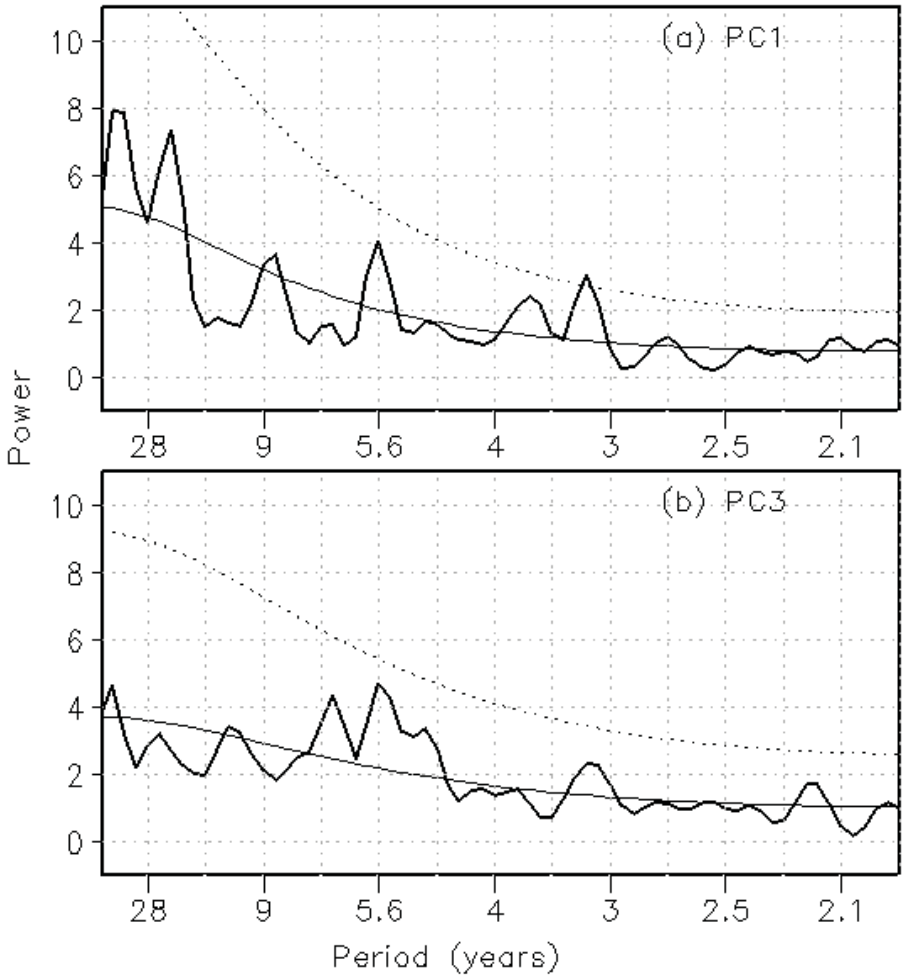

Figure 4. Power spectrum of the (a) PC1 and (b) PC3 of EOF modes of observational SST for the period 1817-2011. Thin solid line is spectrum of best-fit AR1 process and dotted line is associated 10% confidence level.

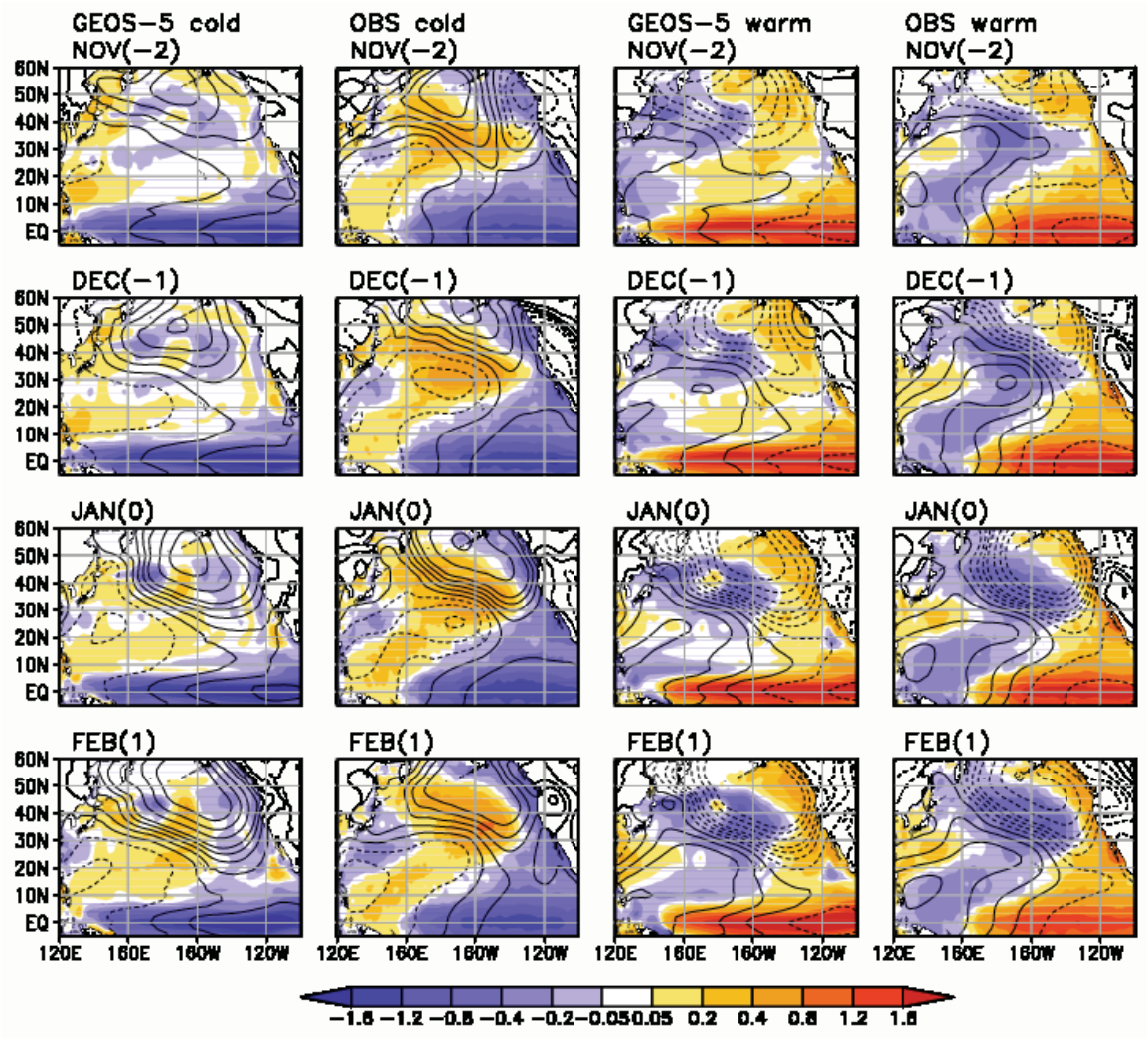

Figure 5. Cold and warm composites of monthly SST (shading) and SLP (contour) anomalies based on DJF Nino3 index based on (columns 1 and 3, from left) model simulation (350 years) and (columns 2 and 4 from left) for Hadley Centre SST and NOAA 20th Century Reanalysis SLP (1871-2010). Months are noted in panel labels and the numbers in bracket denote number of months leading or lagging from January. Contour levels are +(-) 4, 3, 2, 1.5, 1, 0.5 and 0. Dotted lines represent negative contours.

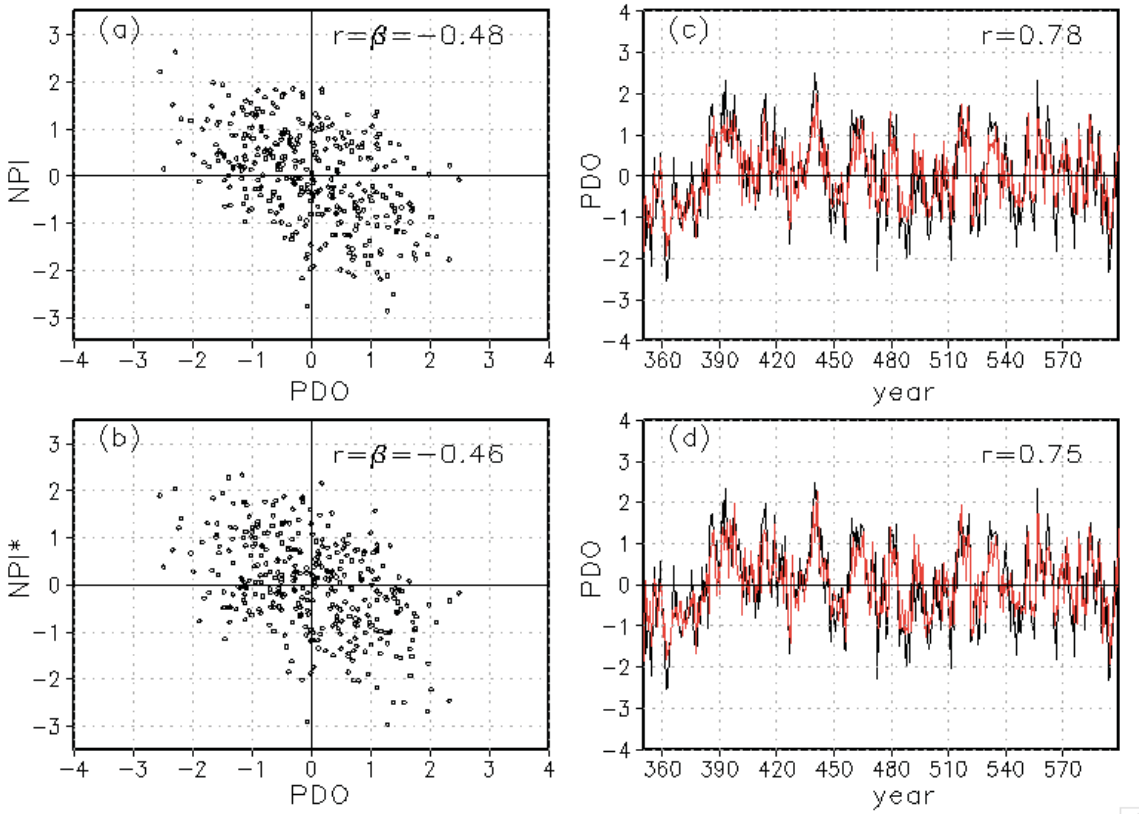

Figure 6. Scatter plot of the PC1 of the DJF SST anomalies (PDO index) against (a) North Pacific Index (NPI) and (b) against the revised NPI that is obtained after removing the ENSO signal by linear regression (NPI*). The right panels show the PDO index (black curve in c, d) and their respective AR1 forecasts (red curve in c, d) (c) using the total NPI and (d) using the NPI*. Correlation coefficients between PDO and the NPI or NPI* form the β parameter for the AR1 forecasts in (c, d). All data are from the model simulation.

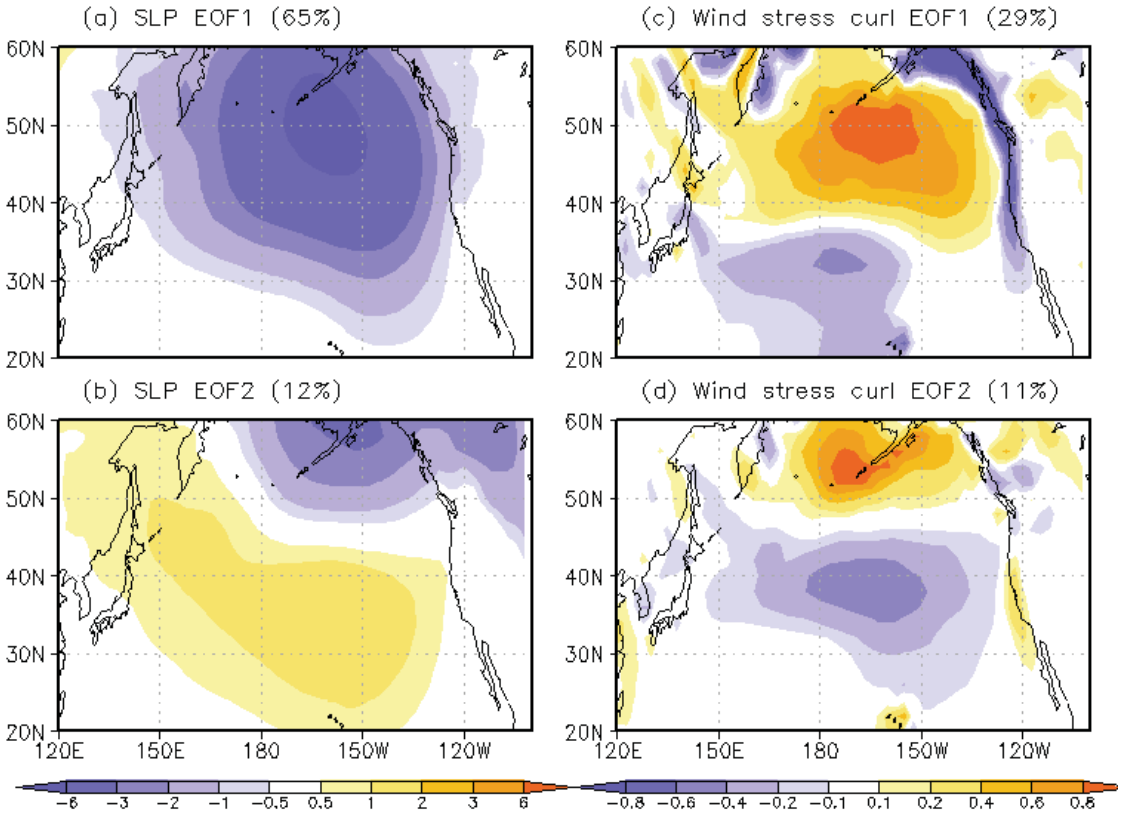

Figure 7. EOFs 1 and 2 of DJF (left) SLP and (right) wind stress curl anomalies for the model simulation. Percentage of variance (noted in plot labels) is based mean variance of 8.8 for SLP and 3.9E-5 for wind stress curl. The EOFs are multiplied by the standard deviation of the PCs to have units (a, b) hPa and (c,d) $Nm^{-3}10^{-7}$.

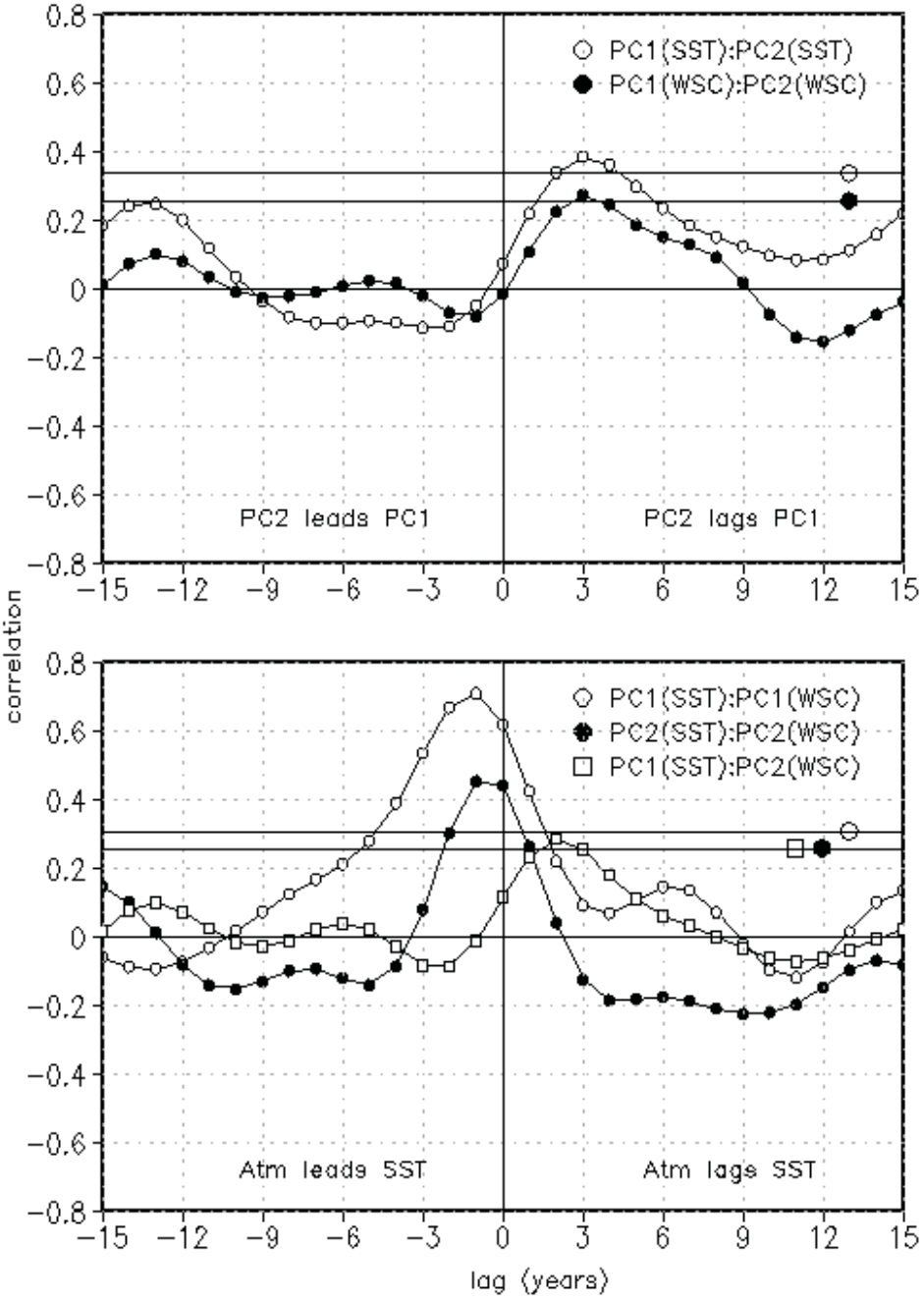

Figure 8. The (top) lead/lag correlation between the (open circle) PC1 and PC2 of SST and (closed circle) PC1 and PC2 of wind stress curl. The (bottom) Lead/lag correlation between (open circle) PC1 of SST and PC1 of wind stress curl, (closed circle) PC2 of SST and PC2 of wind stress curl and (open square) PC1 of SST and PC2 of wind stress curl. Negative lags in the top panel indicate PC1 leads PC2 and in the bottom panel atmosphere leads SST. Horizontal lines with a symbol represent 5% significance level for based on two-sided t-test. Since only positive correlation coefficients are discussed, significance level is noted only for that. All time series are 6-year low pass filtered. All data are from the model simulation.

1020

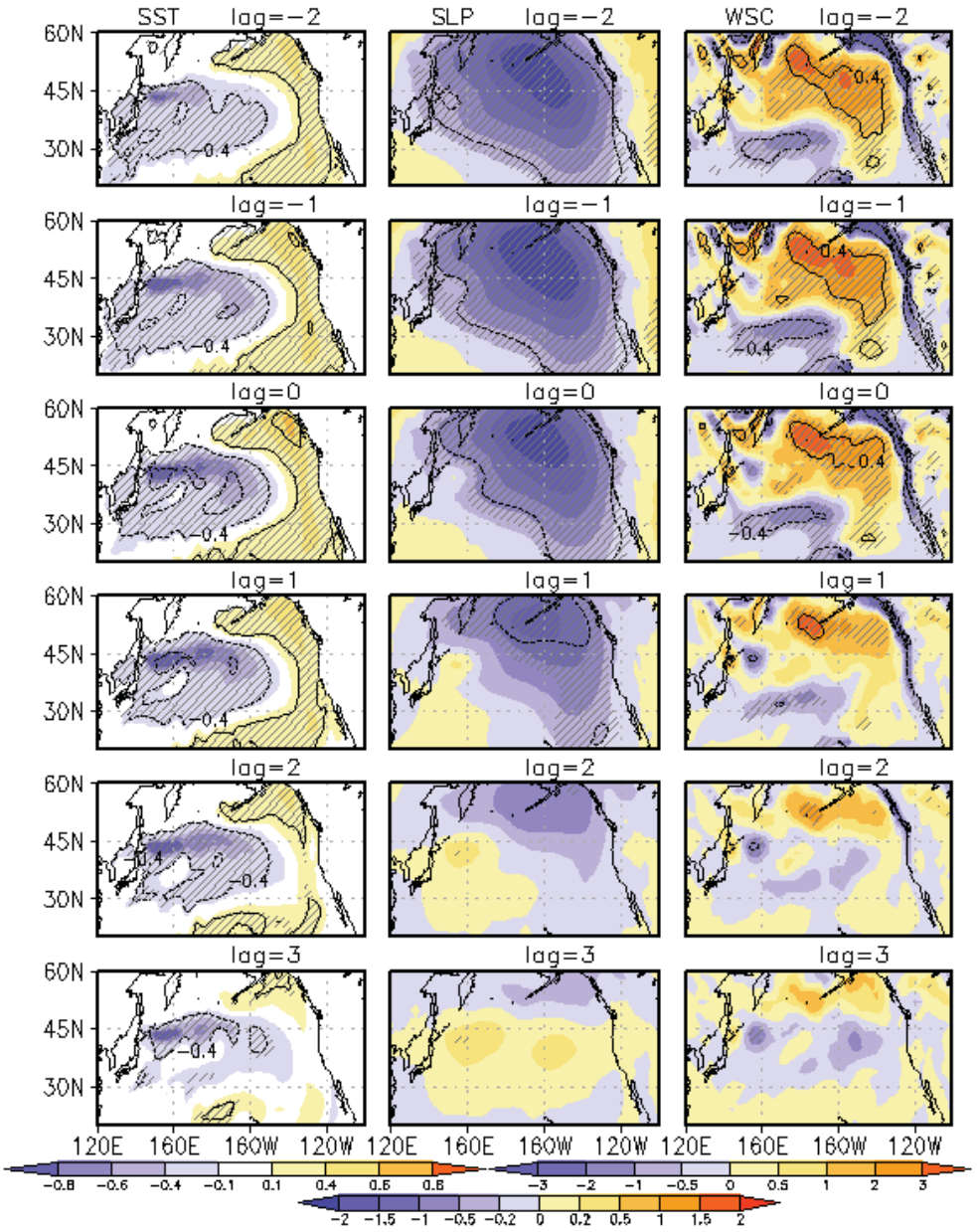

1021
1022 Figure 9. Lead/Lag regressions (shading) and correlations (contours) of (column 1) SST
1023 (°C), (column 2) SLP (hPa) and (column 3) wind stress curl (10^{-8} Nm^{-3}) w.r.t the
1024 normalized PC1 of SST (i.e., PDO index). Lags are in years. Negative (positive) lag
1025 indicates PDO lags (leads) the field. All variables are from the model simulation and are
1026 6-year low pass filtered. Hatching indicates significance at 5% level from a two-sided t-
1027 test.
1028

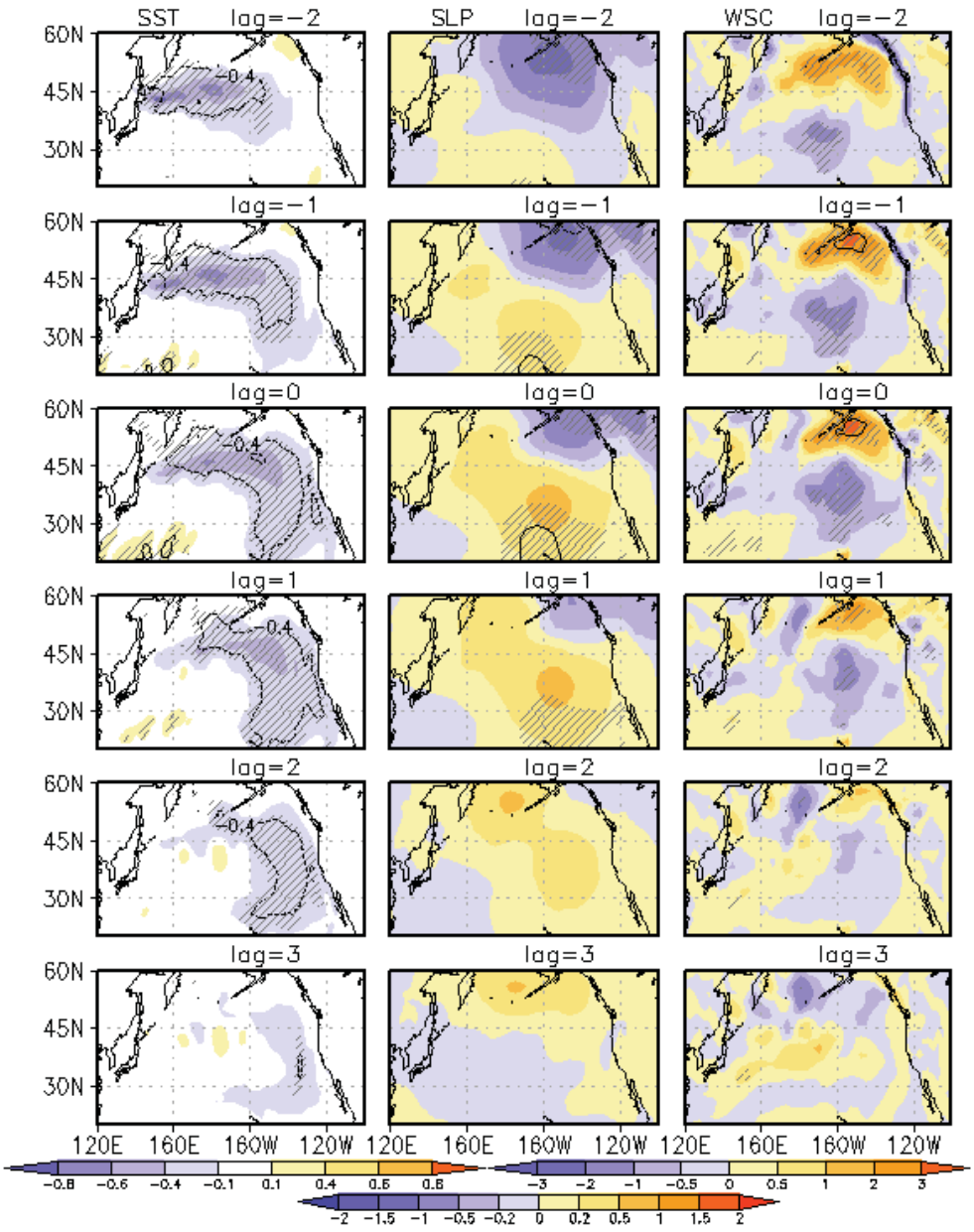

Figure 10. Same as Fig. 9: but w.r.t the PC2 of the SST or the NPGO index.

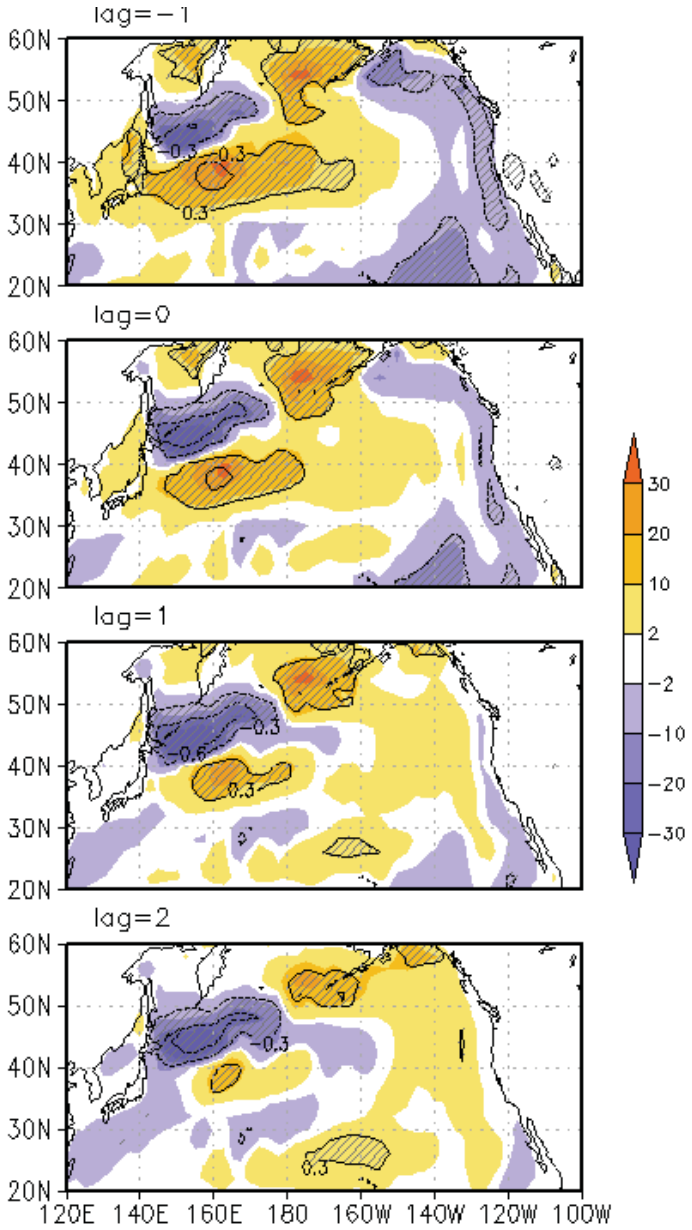

Figure 11. Lead/lag regressions (shading) and correlations (contours) of the net surface heat flux (Wm^{-2} per °C) with respect to the KOE index. Positive net heat flux is directed into the ocean. Hatching indicates 5% significance level based on a two-sided t-test.

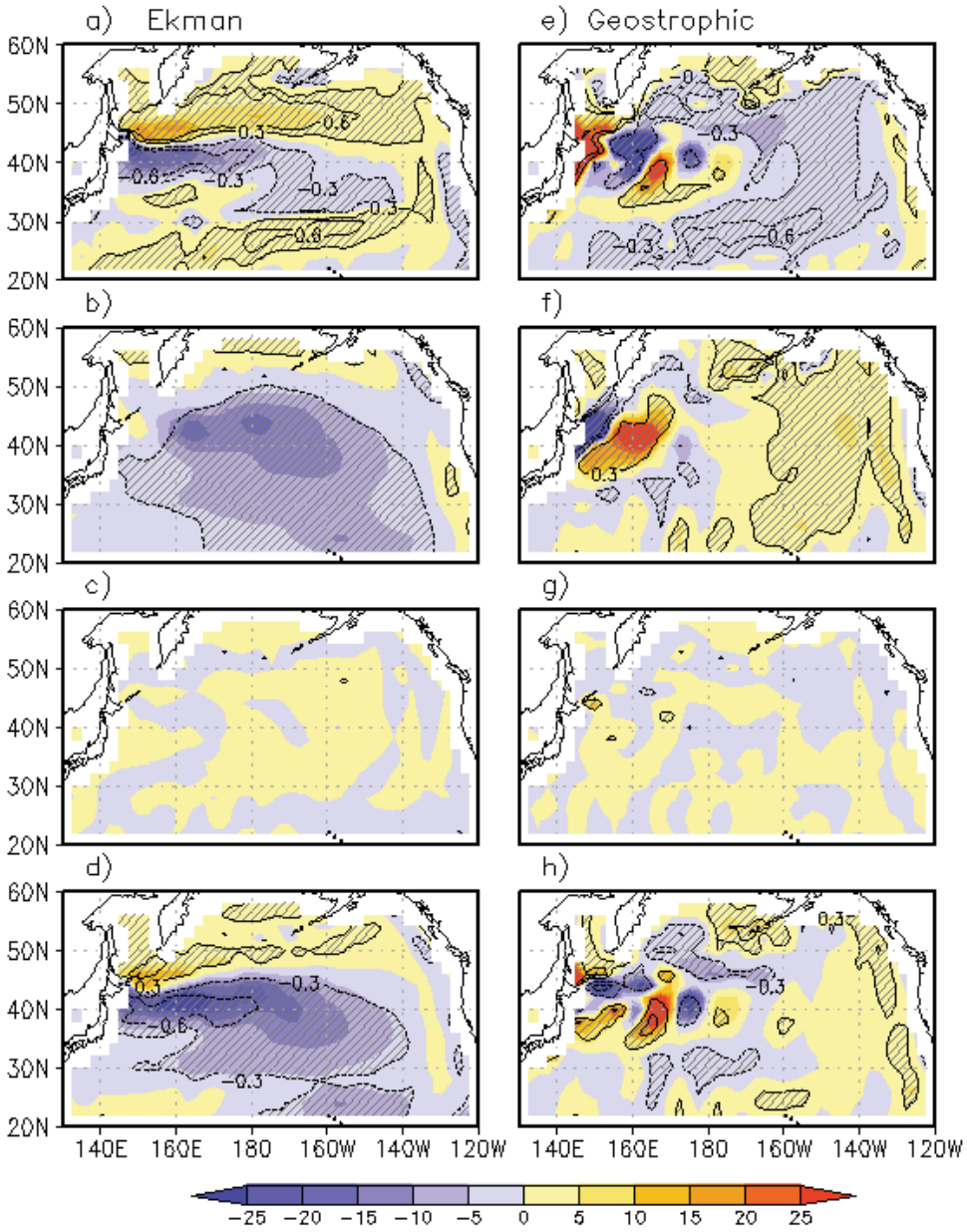

Figure 12. Simultaneous regressions (shading) and correlations (contours) of temperature advection by (left column) Ekman and (right column) geostrophic currents in the mixed layer (Wm^{-2} per °C) with respect to the KOE index. The anomalous transport is decomposed into (a, e) advection of temperature anomaly by mean currents or $\overline{\boldsymbol{V}} \cdot \boldsymbol{\nabla} T'$, (b, f) advection of mean temperature by anomalous currents or $\mathbf{V}' \cdot \boldsymbol{\nabla} \overline{T}$, (c, g) advection of temperature anomaly by anomalous currents or $\boldsymbol{V}' \cdot \boldsymbol{\nabla} T'$, and (d, h) sum of all three or total anomalous transport, where $\boldsymbol{V}$ stands for total Ekman or geostrophic velocity vector in the mixed layer. The overbar denotes climatological mean and prime denotes deviation from climatology. Hatching indicates 5% significance level.